

The effect of Zr-substitution in $\text{La}_{1-x}\text{Sr}_x\text{Co}_{0.2}\text{M}_{0.6}\text{Zr}_{0.2}\text{O}_{3-\delta}$ (M=Fe, Mn) on the crystal structure, thermal expansion and electronic transport properties

Vegar Øygarden^{1)*} and Tor Grande¹⁾

¹⁾ Department of Materials Science and Engineering, NTNU Norwegian University of Science and Technology, NO-7491 Trondheim, Norway

Keywords: Perovskite; Zr-substitution; X-ray diffraction; Electrical conductivity; Thermal expansion.

*Corresponding author: vegar.oygarden@gmail.com

Abstract

The effect of Zr-substitution on the evolution of crystal structure, thermal expansion and the electronic transport properties is reported for $\text{La}_{1-x}\text{Sr}_x\text{Co}_{0.2}\text{Fe}_{0.6}\text{Zr}_{0.2}\text{O}_{3-\delta}$ ($0.1 \leq x \leq 1.0$) and $\text{La}_{1-x}\text{Sr}_x\text{Co}_{0.2}\text{Mn}_{0.6}\text{Zr}_{0.2}\text{O}_{3-\delta}$ ($x = 0.1, 0.2, 0.25, 0.3$). $\text{La}_{1-x}\text{Sr}_x\text{Co}_{0.2}\text{Fe}_{0.6}\text{Zr}_{0.2}\text{O}_{3-\delta}$ was found to be single-phase for the compositions investigated. The electrical conductivity of $\text{La}_{1-x}\text{Sr}_x\text{Co}_{0.2}\text{Fe}_{0.6}\text{Zr}_{0.2}\text{O}_{3-\delta}$ demonstrated a maximum for $x = 0.5$, while the area specific resistance was shown to decrease significantly with increasing Sr-content due to an increased concentration of oxygen vacancies. No signs of oxygen vacancy ordering were observed. The area specific resistance of $\text{La}_{0.3}\text{Sr}_{0.7}\text{Co}_{0.2}\text{Fe}_{0.6}\text{Zr}_{0.2}\text{O}_{3-\delta}$ at 600 °C is close to an order of magnitude lower than reported values for $\text{La}_{0.4}\text{Sr}_{0.6}\text{Co}_{0.2}\text{Fe}_{0.8}\text{O}_{3-\delta}$. The series $\text{La}_{1-x}\text{Sr}_x\text{Co}_{0.2}\text{Mn}_{0.6}\text{Zr}_{0.2}\text{O}_{3-\delta}$ was found as multiphase materials. The stability of both series is discussed with respect to the red-ox properties of the transition metals.

Introduction

Intermediate temperature solid oxide fuel cells (IT-SOFC) have received significant attention in recent years as the search for green energy converters has become more relevant. Lower operating temperature allows the use of metallic interconnects, whilst also improving material compatibility and sealing [1]. The development of these fuel cells are limited due to the lack of efficient cathode materials at lower operating temperatures [2]. New materials which combine high electronic and ionic conductivity with chemical phase stability, high catalytic activity for oxygen reduction, and moderate thermal expansion is of high scientific and technological interest.

$\text{La}_{1-x}\text{Sr}_x\text{Co}_{1-y}\text{Fe}_y\text{O}_{3-\delta}$ has been extensively investigated as a potential cathode material in SOFCs [3-7]. Both the ionic and electronic conductivity is shown to increase with increasing Sr-content due to the formation of electron holes and oxygen vacancies [5]. The ionic conductivity reaches a maximum for Sr-content equal to ~ 0.5 . For high Sr-concentrations it is reported that the oxygen vacancies order and form defect clusters, which severely reduces the ionic conduction due to an increased activation barrier for ionic transport [8-10].

In perovskites, B-site substitution of high valence cations such as Zr^{4+} , Nb^{5+} and Ta^{5+} has been shown to increase structural stability whilst simultaneously reducing thermal expansion [11, 12]. These cations bond strongly to their surrounding oxygen sites due to the high and stable valence state, which results in short bond-length thereby inducing local structural perturbations of the perovskite BO_6 octahedra. These distortions are suggested to prevent long-range ordering of oxygen vacancies which could inhibit defect clustering. Retaining high vacancy concentration, whilst simultaneously avoiding vacancy ordering is crucial in order to achieve a high rate of oxygen ion diffusion.

Zr^{4+} , Nb^{5+} and Ta^{5+} have no d-electrons, and will therefore not contribute to the electronic conductivity, however, the highly stable oxidation states enables tuning of the oxidation states of other B-cations through the effect of electroneutrality. This in turn makes it possible to optimize the electronic properties.

Here we report on the crystal structure, electrical transport and thermal expansion in the solid solution series of $\text{La}_{1-x}\text{Sr}_x\text{Co}_{0.2}\text{Fe}_{0.6}\text{Zr}_{0.2}\text{O}_{3-\delta}$ ($0.1 < x < 1.0$) and $\text{La}_{1-x}\text{Sr}_x\text{Co}_{0.2}\text{Mn}_{0.6}\text{Zr}_{0.2}\text{O}_{3-\delta}$ (0.1, 0.2, 0.25, 0.3). First, we report on how the crystal structure and the electrical properties of the two material systems change with Sr-content. Moreover, the study explores how Zr-substitution effects on oxygen vacancy ordering and optimization of the electrical properties through tuning of oxygen vacancy concentration and the oxidation states of Fe and Co.

Experimental

Solid solutions of the two series $\text{La}_{1-x}\text{Sr}_x\text{Co}_{0.2}\text{Fe}_{0.6}\text{Zr}_{0.2}\text{O}_{3-\delta}$ (0.1 – 1.0) and $\text{La}_{1-x}\text{Sr}_x\text{Co}_{0.2}\text{Mn}_{0.6}\text{Zr}_{0.2}\text{O}_{3-\delta}$ (0.1, 0.2, 0.25, 0.3) were prepared using a solid-state synthesis route. Stoichiometric amounts of La_2O_3 (Sigma Aldrich, > 99.99%), SrCO_3 (Sigma Aldrich > 99.9%), Co_3O_4 (Sigma Aldrich, > 99.9%), ZrO_2 (Sigma Aldrich, > 99.9%), Fe_2O_3 (Sigma Aldrich, > 99.9%) and MnO_2 (Sigma Aldrich, > 99.9%) were mixed in 100% ethanol and ball milled at 60 rpm for 24 hours. La_2O_3 was dried at 800 °C overnight prior to use. 250mL plastic bottles were used with the grinding media occupying between 1/3 and 1/2 of the bottle volume. The grinding

media was balls of zirconia ceramics with 5 mm diameter. The ground powder mixtures were calcined at 1000 - 1100 °C for 12 hours, and sieved through a 250 µm mesh. Dense materials were obtained by uniaxial pressing (20 MPa) the powders into the desired shape, followed by heat treatment at 1350 - 1450 °C in air for 6 hours to achieve densities greater than 93% of theoretical density with grain sizes in the range of 1 – 20 µm.

The X-ray powder diffraction patterns were collected using a Bruker D5005 A-unit equipped with Cu-radiation and a primary monochromator. Data was collected from 15 – 130° with step size 0.012° and counting time 8 seconds per step. The diffraction patterns were fitted in Topas v4.2 using a Thompson-Cox-Hastings pseudo-Voigt peak model and Chebychev background model with 5 orders.

Electronic conductivity was determined using a four-point DC method on densely sintered rectangular bar samples sized 5 x 10 x 50 mm. Constant current of 0.1 A was used on all samples. The samples were measured in two consecutive runs from room temperature to 1000 °C. The area specific resistance (ASR) of $\text{La}_{1-x}\text{Sr}_x\text{Co}_{0.2}\text{Fe}_{0.6}\text{Zr}_{0.2}\text{O}_{3-\delta}$ ($x = 0.5, 0.7$) was measured using high-temperature electronic impedance spectroscopy on symmetrical cells. A densely sintered sample of $\text{Ce}_{0.9}\text{Gd}_{0.1}\text{O}_{2-\delta}$ was used as electrolyte, and the cathode materials were sprayed onto the electrolyte using a Sono-Tek spray coater equipped with a heating plate set to 70 °C. An infusion rate of 0.3 mL/min was used to apply 50 – 200 µm thick layers onto both sides of the electrolyte, before sintering the cell for 2 hours at 1025 °C. The cells were mounted using the ProboStat™ sample holder setup for circular discs and the impedance signal was analysed using an Alpha-A High Performance Frequency Analyser from Novocontrol. A typical impedance measurement covered the frequency range from 1 MHz to 10 mHz. An Ac-amplitude of 50 mV was used throughout the experiments. The impedance was modelled to an equivalent circuit using the ZSimpWin v3.21 software.

The thermal expansion of the materials was determined using a Netzsch DIL 402C dilatometer in air. 10 mm long cylindrical samples with 5 mm diameter sintered in air were polished to ensure parallel ends. The instrument was calibrated using an aluminium reference sample of known length. The thermal expansion coefficient was extracted using the Proteus analysing software.

Results

The X-ray diffraction (XRD) patterns of the solid solution series $\text{La}_{1-x}\text{Sr}_x\text{Co}_{0.2}\text{Fe}_{0.6}\text{Zr}_{0.2}\text{O}_{3-\delta}$ (LSCFZ) are presented in Figure 1. The diffraction pattern of $x = 0.1$ correlates to the $a^-a^+c^+$ tilt system. The lack of intensity at the $0kl$ ($k = 2n + 1$) reflections meant the material could be indexed to the orthorhombic $Pbnm$ space group. The superreflections stemming from the orthorhombic superlattice are shown in the figure. The odd-odd-odd (R-point reflections) and even-even-odd reflections (X-point reflections stemming from simultaneous presence of both M- and R-points) decrease in intensity with increasing x . The R- and X-point reflections are no longer present for $x = 0.3$, although the 103 reflection is still observable. The absence of other superreflections suggests a higher symmetry orthorhombic or tetragonal structure such as $Ibmm$ (No. 74), $P4/mbm$ (No. 127) or $I4/mcm$ (No. 140). The Rietveld refinement gave the best fit to orthorhombic $Ibmm$, but neutron diffraction or synchrotron X-ray diffraction data would be needed to determine the space group unambiguously. For $x = 0.6$, the intensity of the 103

diffraction peak is no longer present, and the material is indexed to cubic $Pm\bar{3}m$. The lattice parameters are summarised in Table 1.

The pseudocubic lattice parameters of LSCFZ are presented in Figure 2. The unit cell parameters decrease with increasing Sr-content for $x = 0.1$ to $x = 0.6$. The unit cell volume of $x = 0.7$ is similar to $x = 0.6$, and for higher values of x , the unit cell volume increases. The initial decrease of the unit cell is due to oxidation of Fe and Co as La^{3+} is substituted by Sr^{2+} , as described using Kröger-Vink notation [13] in Eq. (1).

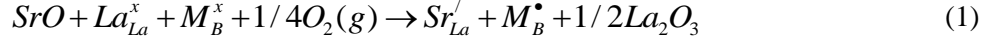


Table 1. The average TEC between 100 – 700 °C, the electrical conductivity at 700 °C and the crystallographic data for $La_{1-x}Sr_xCo_{0.2}Fe_{0.6}Zr_{0.2}O_{3-\delta}$ ($0.1 \leq x \leq 1$). R_{wp} describes the quality of the Rietveld refinements.

		x = 0.1	x = 0.2	x = 0.3	x = 0.4	x = 0.5
TEC ($10^{-6} K^{-1}$)		-	-	-	14.4	16.4
σ (S/cm) (700 °C)		0.65	2.16	16.9	22.4	83.1
Space group		<i>Pbnm</i>	<i>Pbnm</i>	<i>Ibmm</i>	<i>Ibmm</i>	<i>Ibmm</i>
a (Å)		5.5951(1)	5.5810(2)	5.5836(2)	5.5837(2)	5.5691(4)
b (Å)		5.6102(1)	5.5781(2)	5.5680(2)	5.5563(2)	5.5458(3)
c (Å)		7.9162(2)	7.8906(3)	7.8777(3)	7.8660(3)	7.8683(5)
R_{wp}		2.8	2.7	2.6	2.7	3.0
La	x	0.4959(1)	0.4952(1)	0.4947(6)	0.4981(8)	0.5015(8)
	y	0.4740(1)	0.4805(1)	1/2	1/2	1/2
O1	x	0.567(4)	0.559(4)	0.558(4)	0.550(4)	0.517(8)
	y	0.020(2)	0.021(3)	0	0	0
O2	x	0.274(3)	0.255(3)	1/4	1/4	1/4
	y	0.727(3)	0.704(3)	3/4	3/4	3/4
	z	0.052(2)	0.045(2)	0.041(2)	0.042(1)	0.049(2)
		x = 0.6	x = 0.7	x = 0.8	x = 0.9	x = 1.0
σ (S/cm) (700 °C)		40.4	20.6	-	10.2	5.4
Space group		$Pm\bar{3}m$	$Pm\bar{3}m$	$Pm\bar{3}m$	$Pm\bar{3}m$	$Pm\bar{3}m$
a (Å)		3.9243(1)	3.9243(1)	3.9288(1)	3.9294(1) O ₂ : 3.9200(1)	3.9339

Rwp(%)	3.7	2.8	2.9	3.4	1.9
--------	-----	-----	-----	-----	-----

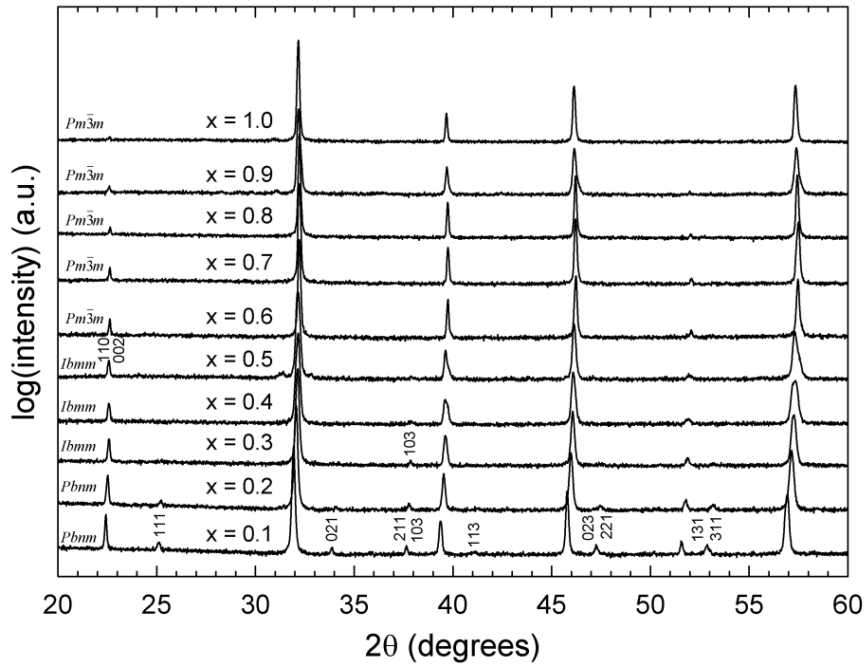


Figure 1. X-Ray diffraction patterns of $\text{La}_{1-x}\text{Sr}_x\text{Co}_{0.2}\text{Fe}_{0.6}\text{Zr}_{0.2}\text{O}_{3-\delta}$ ($0.1 \leq x \leq 1.0$). The superreflections stemming from orthorhombic $Pbnm$ and $Ibmm$ symmetry are highlighted.

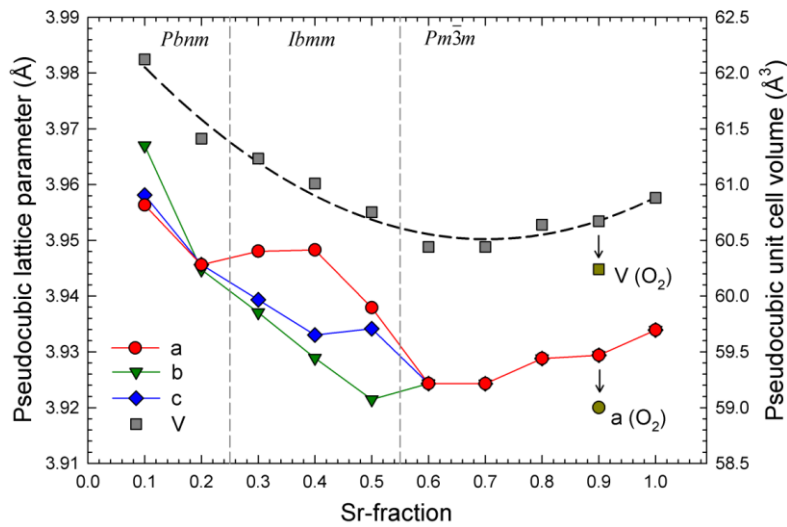


Figure 2. Pseudocubic lattice parameters and the unit cell volume of the $\text{La}_{1-x}\text{Sr}_x\text{Co}_{0.2}\text{Fe}_{0.6}\text{Zr}_{0.2}\text{O}_{3-\delta}$ materials. The dotted line is a guide to the eye.

Upon further Sr-substitution, the oxidation state of Fe and Co reaches a critical value where it is energetically more favourable to form oxygen vacancies rather than further oxidation of Co/Fe according Eq. (2). The increase in lattice volume seen in Figure 2 for $x > 0.7$ is due to the larger ionic size Sr^{2+} (1.40 Å) compared to La^{3+} (1.36 Å).



Any further Sr-substitution after this point will further increase the oxygen vacancy concentration. The concentration of oxygen vacancies is highly $p\text{O}_2$ -dependent, which is made evident by re-heating $x = 0.9$ in oxygen at $800\text{ }^\circ\text{C}$. As seen in Figure 3, the unit cell parameters and volume decrease significantly as the material was oxidised at $800\text{ }^\circ\text{C}$.

The electrical conductivity of LSCFZ is presented in Figure 3. The conductivity increases with increasing Sr-substitution up to $x = 0.5$, after which further substitution decreases the conductivity, in line with previous reports of similar systems. $x = 0.1$ and 0.2 demonstrate semiconducting charge transport in the entire temperature interval, while the materials from $x = 0.3$ to $x = 1$ exhibit an apparent, gradual change from a semi-conductor to an apparently metallic behaviour. For $x = 1$, the change in the slope is seen at $\sim 400\text{ }^\circ\text{C}$ while at higher temperatures the materials appear to revert back to semiconducting behaviour as an increase in conductivity is seen with increasing temperature at high temperatures. No data was recorded for $x = 1$ above $\sim 850\text{ }^\circ\text{C}$ due to sample-detachment. Table 1 summarises the conductivity at $700\text{ }^\circ\text{C}$ for all the materials.

Figure 4 shows the electrical conductivity plotted in isotherms from $400 - 900\text{ }^\circ\text{C}$ as a function of Sr-content. The maximum conductivity is found for $x = 0.5$ for all isotherms. The insert in Figure 4 presents the temperature at which the slope of conductivity versus temperature changes sign. The transition temperature decreases roughly linearly as a function of Sr-content before it increases for $x = 0.9$ and $x = 1$. This is related to the increased unit cell volume due to the increased concentration of oxygen vacancies as described earlier.

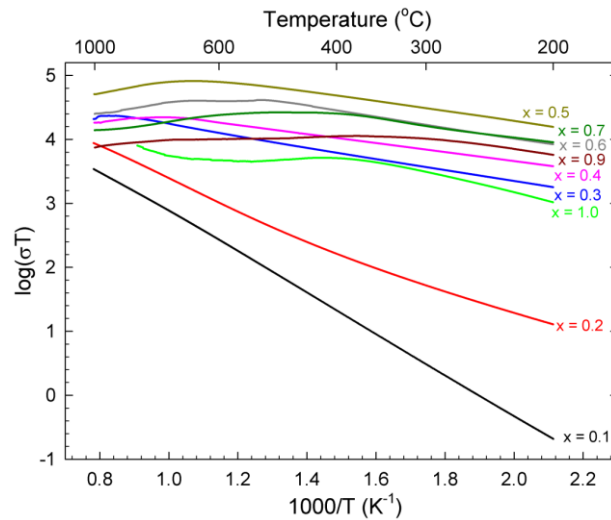


Figure 3. $\log(\sigma T)$ of $\text{La}_{1-x}\text{Sr}_x\text{Co}_{0.2}\text{Fe}_{0.6}\text{Zr}_{0.2}\text{O}_{3-\delta}$ materials plotted as a function of reciprocal temperature.

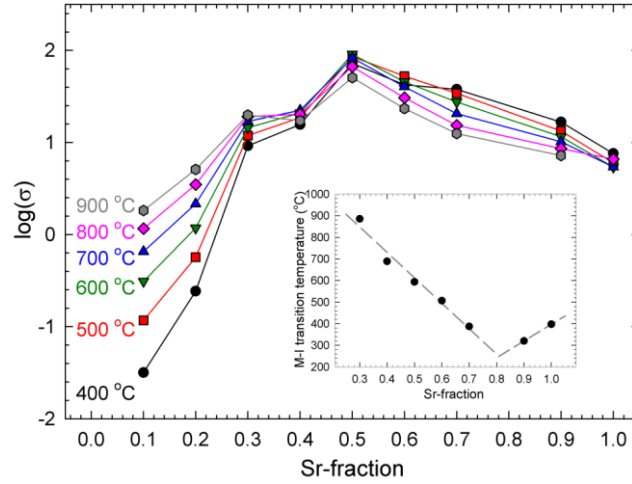


Figure 4. $\log(\sigma)$ for the materials $\text{La}_{1-x}\text{Sr}_x\text{Co}_{0.2}\text{Fe}_{0.6}\text{Zr}_{0.2}\text{O}_{3-\delta}$, given as a function of Sr-content in the temperature range 400 – 900 °C. Insert shows the apparent metal-insulator transition temperature as a function of Sr-content.

The area specific resistance (ASR) of the two most promising materials LSCFZ ($x = 0.5$ and 0.7) was collected by high-temperature impedance and plotted as a function of reciprocal temperature in Figure 5. Values for $\text{La}_{0.4}\text{Sr}_{0.6}\text{Co}_{0.2}\text{Fe}_{0.8}\text{O}_{3-\delta}$ (LSCF4628) are collected from [14] and used in comparison. $x = 0.7$ is shown to exhibit significantly lower ASR than $x = 0.5$ for the whole temperature interval, contrary to what would be expected if only the electrical conductivities were considered (see Figure 4). The ASR of $x = 0.7$ are comparable to LSCF4628 at 750 °C, while a significantly lowered ASR is demonstrated at lower temperatures. The activation energy for $x = 0.7$, which is proportional to the slope, is also seen to be lower than both $x = 0.5$ and LSCF4628. Selected ASR values and activation energies are given in Table 2.

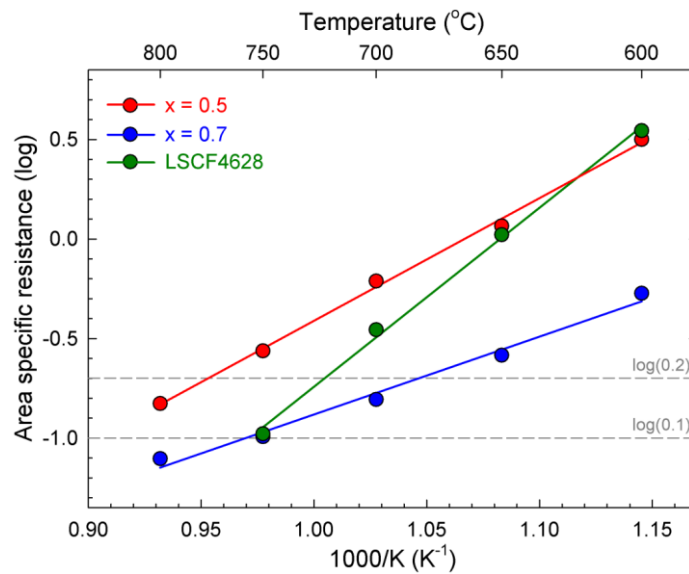


Figure 5. Area specific resistance of $\text{La}_{1-x}\text{Sr}_x\text{Co}_{0.2}\text{Fe}_{0.6}\text{Zr}_{0.2}\text{O}_{3-\delta}$ ($x = 0.5$ and 0.7) compared to $\text{La}_{0.4}\text{Sr}_{0.6}\text{Co}_{0.2}\text{Fe}_{0.8}\text{O}_{3-\delta}$. Data for the latter is collected from [14]. $\log(0.1)$ and $\log(0.2)$ are highlighted as reference points.

Table 2. Area specific resistance (ASR) and activation energies for $\text{La}_{1-x}\text{Sr}_x\text{Co}_{0.2}\text{Fe}_{0.6}\text{Zr}_{0.2}\text{O}_{3-\delta}$ ($x = 0.5$ and 0.7) as compared to $\text{La}_{0.4}\text{Sr}_{0.6}\text{Co}_{0.2}\text{Fe}_{0.8}\text{O}_3$ (LSCF). Data for LSCF collected from [14].

	$x = 0.5$	$x = 0.7$	LSCF
ASR (Ωcm^2 , $T=600\text{ }^\circ\text{C}$)	3.16	0.53	3.50
ASR (Ωcm^2 , $T=750\text{ }^\circ\text{C}$)	0.27	0.10	0.11
E_a (eV)	0.53	0.34	0.78

The linear thermal expansion, measured by dilatometry, of the two most promising materials LSCFZ ($x = 0.4$ and 0.5) is shown in Figure 6. The thermal expansion is shown to increase significantly at $\sim 450\text{ }^\circ\text{C}$ due to the contribution of chemical expansion. This is reflected in Figure 7 where the TEC of $x = 0.4$ and $x = 0.5$ is plotted as a function of temperature. The TEC of both materials increases significantly from ~ 450 to $900\text{ }^\circ\text{C}$ as a response to the increasing concentration of oxygen vacancies giving rise to chemical expansion. The TEC curves of both materials are similar, although the curve of $x = 0.4$ was shifted towards lower TEC as reflected by an average TEC of 14.4 in the temperature range $100 - 700\text{ }^\circ\text{C}$, while $x = 0.5$ had an average TEC of 16.4 .

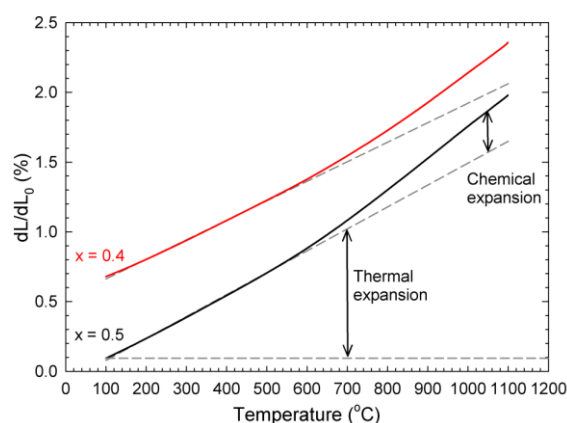


Figure 6. The linear thermal expansion of $\text{La}_{1-x}\text{Sr}_x\text{Co}_{0.2}\text{Fe}_{0.6}\text{Zr}_{0.2}\text{O}_{3-\delta}$ ($x = 0.4$ and 0.5) measured by dilatometry in air and plotted as a function of temperature. The curve for $x = 0.4$ is shifted on the y-scale to increase readability.

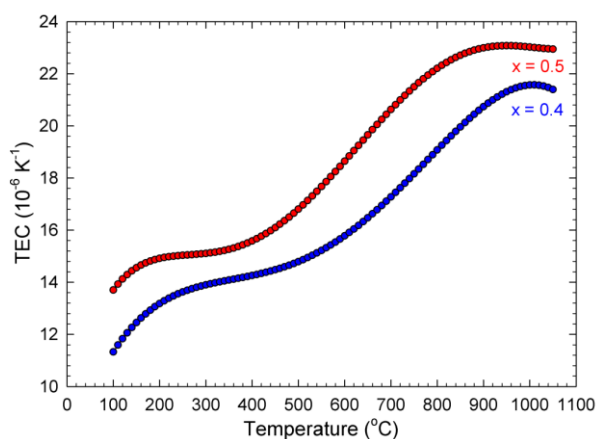


Figure 7. The thermal expansion coefficient (TEC) of $\text{La}_{0.6}\text{Sr}_{0.4}\text{Co}_{0.2}\text{Fe}_{0.6}\text{Zr}_{0.2}\text{O}_{3-\delta}$ and $\text{La}_{0.5}\text{Sr}_{0.5}\text{Co}_{0.2}\text{Fe}_{0.6}\text{Zr}_{0.2}\text{O}_{3-\delta}$ plotted as a function of temperature.

XRD patterns of $\text{La}_{1-x}\text{Sr}_x\text{Co}_{0.2}\text{Mn}_{0.6}\text{Zr}_{0.2}\text{O}_{3-\delta}$ ($x = 0.1, 0.2, 0.25, 0.3$) (LSCMZ) are presented in Figure 8. The major phase found was a perovskite, but secondary phases, $\text{La}_2\text{Zr}_2\text{O}_7$, SrZrO_3 , or both, were always formed irrespective of the value of x . The phase fractions of all materials are plotted as a function of Sr-content in Figure 9. For $x = 0.1$ and 0.3 , the perovskite phase was indexed to orthorhombic $Pbnm$ based on the observed superreflections. For $x = 0.1$, a secondary phase of $\text{La}_2\text{Zr}_2\text{O}_7$ was found, whilst for $x = 0.3$, the secondary phase present was SrZrO_3 . For $x = 0.2$ and $x = 0.25$, the diffraction patterns of the perovskite phase could only be described using both rhombohedral $R\bar{3}c$ and orthorhombic $Pbnm$, as described in more detail in [15, 16]. Rietveld refinements suggested the rhombohedral phase was dominating for $x = 0.2$, while the orthorhombic phase was dominating for $x = 0.25$. $\text{La}_2\text{Zr}_2\text{O}_7$ and SrZrO_3 was found for both materials, with the former dominating for $x = 0.2$ and the latter dominating for $x = 0.25$. Both $x = 0.2$ and $x = 0.25$ were also heat treated in N_2 at $1350\text{ }^\circ\text{C}$ for 12 hours. The phase fractions showed increasing fraction of SrZrO_3 and decreasing fraction of $\text{La}_2\text{Zr}_2\text{O}_7$ as compared to the materials heated in air.

The work on LSCMZ was terminated at this point due to the inability to produce single-phase materials. The origin of the instability of LSCMZ as compared to LSCFZ will be treated in detail further below.

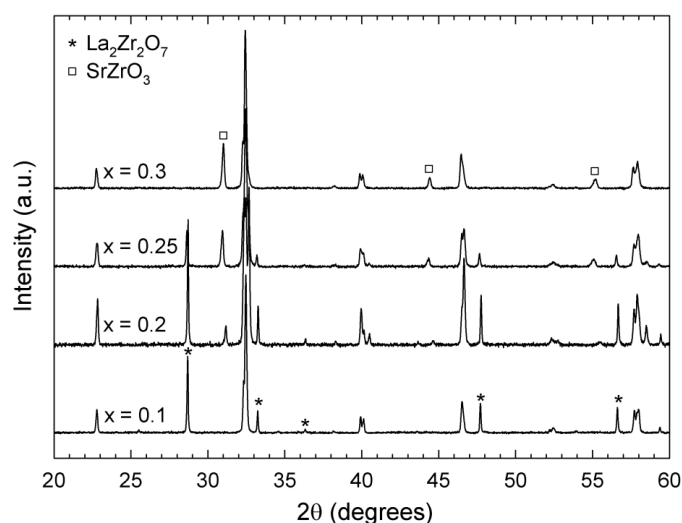


Figure 8. The XRD pattern of $\text{La}_{1-x}\text{Sr}_x\text{Co}_{0.2}\text{Mn}_{0.6}\text{Zr}_{0.2}\text{O}_{3-\delta}$ ($x = 0.1, 0.2, 0.25$ and 0.3). (*) indicates the diffraction peaks of $\text{La}_2\text{Zr}_2\text{O}_7$, while (□) denotes the diffraction peaks of SrZrO_3 .

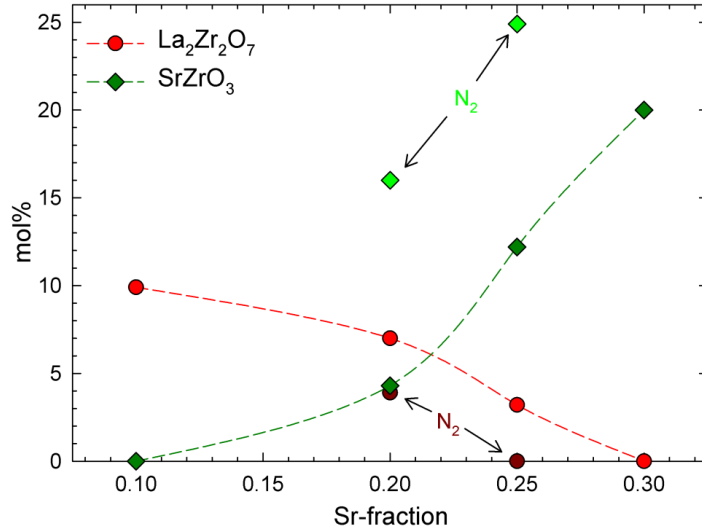


Figure 9. The molar fractions of $\text{La}_2\text{Zr}_2\text{O}_7$ and SrZrO_3 plotted as a function of Sr-content. The phase fractions found by annealing in N_2 is highlighted. The molar fractions are estimated from Rietveld refinements of the XRD patterns.

Discussion

The crystal structure of LSCFZ goes from $Pbnm \rightarrow Ibmm \rightarrow Pm\bar{3}m$ as a function of Sr-content, as seen in Figure 1. Both the phase transitions between the orthorhombic polymorphs and the transition to cubic symmetry are second order according to Howard *et al.* [17]. According to [18], the orthorhombic phase $Ibmm$ is only stable for small octahedral distortions, in line with a Goldschmidt tolerance factor close to one. This correlates well with the calculated tolerance factors for $x = 0.3, 0.4$ and 0.5 which are $\tau = 0.962, 0.966$ and 0.970 , respectively.

The 110 and 002 reflections, seen in Figure 1, diminished with increasing x . This was, however, not due to the phase transitions as these reflections are allowed for all the observed space groups. The intensity of a reflection is determined by the squared sum of the F-factor of the atoms in the plane which gives constructive interference. For the 110 and 002 reflections, the A-ion is in counter-phase with the B- and O-ions. Due to the large size of La, the scattering factor, which describes scattering effect of individual elements, is considerably larger than the average scattering factor of Co, Fe, Zr and O. This leads to an observable intensity at the 110, 002 reflections. As Sr is substituted for La, the average scattering factor of the A-site diminishes since Sr is smaller in size and therefore scatters incoming X-rays less effectively. For $x = 1$, the scattering from the A-site has a similar magnitude as the average scattering from the B- and O-site. This gives destructive interference which almost extinguishes the intensity of the 110 and 002 reflections.

The electrical conductivity of the $\text{La}_{1-x}\text{Sr}_x\text{Co}_{0.2}\text{Fe}_{0.6}\text{Zr}_{0.2}\text{O}_{3-\delta}$ series of materials reached a maximum for $x = 0.5$, see Figure 3 and 4. For $x = 0.1$, no oxygen vacancies are present and the B-site is occupied by a mixture of Co^{2+} , Co^{3+} and Fe^{3+} due to the lower stability of Fe^{2+} relative to Co^{2+} in octahedral configuration in air. For $x = 0.2$, the average oxidation state of Co and Fe

is equal to 3+ if oxygen vacancies are not considered. For higher values of x , a mixed valence of $\text{Co}^{3+}/\text{Co}^{4+}$ and $\text{Fe}^{3+}/\text{Fe}^{4+}$ is introduced which lowers the activation energy for charge transport, assuming polaron hopping is the charge transport mechanism [19, 20]. This is reflected in a steep increase in conductivity clearly seen going from $x = 0.2$ to $x = 0.3$ in Figure 3. The lattice parameters presented in Figure 2 and Table 1 suggest that the oxygen vacancy concentration increases upon further Sr-substitution above $x = 0.5$. From this it can be inferred that the formation of oxygen vacancies is the main charge compensation mechanism rather than by further oxidation of Co and Fe. This lowers the concentration and mobility of the charge carriers, which could explain why the conductivity drops for Sr-substitutions higher than $x = 0.5$.

An apparent gradual insulator to metal (I-M) transition was seen in $\text{La}_{1-x}\text{Sr}_x\text{Co}_{0.2}\text{Fe}_{0.6}\text{Zr}_{0.2}\text{O}_{3-\delta}$ for $x = 0.3 - 1.0$. A rough linear trend was seen for the transition temperature as a function of Sr-content up to $x = 0.7$, as illustrated in the insert in Figure 4. Figure 10 shows the $\log(\sigma)$ as a function of reciprocal temperature, clearly illustrating the transition at the point where the conductivity goes through a maximum. The maximum in conductivity is broad, indicating that it could be related to thermal reduction which lowers the number of charge carriers at elevated temperatures due to loss of oxygen as shown by eq. (2). However, as seen in the insert in Figure 4 the maximum occurs at temperatures around 400 °C for $x = 0.9$ and $x = 1.0$, which is most likely too low for any significant oxygen exchange. The maximum could also be an I-M transition, which is explained from band theory by a broadening of the bands due to increased orbital overlap upon heating. At a given temperature, the Fermi level will be located within the valence band and the charge carriers are regarded as delocalised and the material will be a metallic conductor [21]. For $x = 1$, the material appears to be semiconducting up to the apparent I-M transition at ~ 420 °C, before turning semiconducting again at ~ 530 °C. This is most likely due to a thermally activated increase of oxygen vacancies, which reduces Co and Fe and increases the unit cell volume significantly as seen in Figure 2. The volume increase decreases the orbital overlap and could explain why $x = 1$ reverts back to semiconducting charge transfer at higher temperatures.

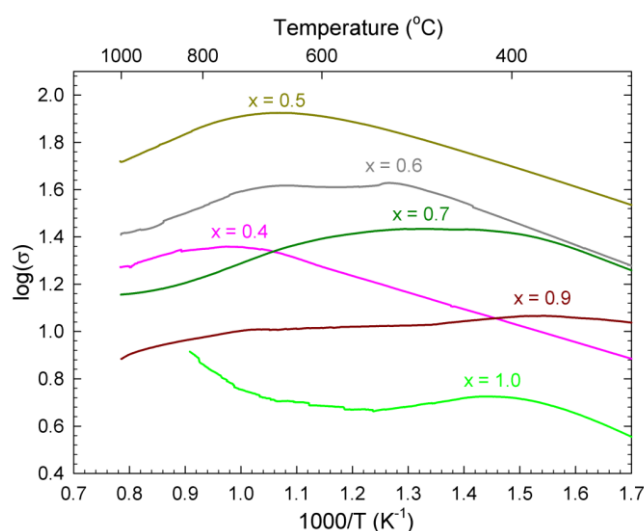
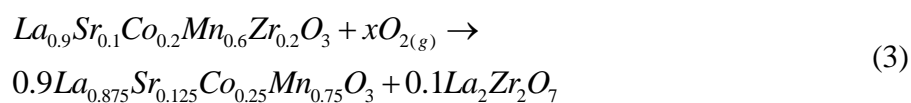


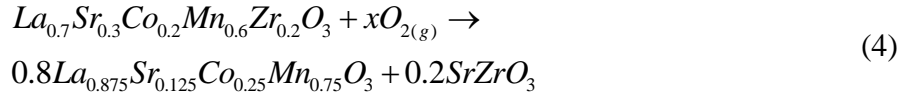
Figure 10. The electrical conductivity plotted as a function of reciprocal temperature for $\text{La}_{1-x}\text{Sr}_x\text{Co}_{0.2}\text{Fe}_{0.6}\text{Zr}_{0.2}\text{O}_{3-\delta}$ ($x = 0.4, 0.5, 0.6, 0.7, 0.9$ and 1.0).

The area specific resistance (ASR) presented in Figure 5 and Table 2 demonstrated significantly lower polarisation resistance for $x = 0.7$ as compared to $x = 0.5$, even though the electrical conductivity of $x = 0.5$ is four times higher than $x = 0.7$ at 700 °C. At 600 °C the ASR of $x = 0.5$ is almost an order of magnitude lower than LSCF4628 which has been extensively studied as a cathode material in IT-SOFCs [14]. These results highlight the importance of high concentrations of randomly disordered oxygen vacancies in order to minimize the ASR. The ASR data shows a linear trend with no signs of vacancy ordering or clustering, which is previously reported to significantly increase polarisation resistance in perovskite type materials with highly oxygen deficient lattice. SrFeO_{3-δ} is a well-known example of oxygen vacancy ordering [22]. The Zr⁴⁺-substitution is proposed to be the reason for the lack of oxygen vacancy ordering due to the local perturbations in the lattice caused by the strong Zr-O oxygen bonds. Zr-substitution also increases lattice stability and decreases thermal expansion and provides a way to manipulate and tailor the oxidation state of the Co and Fe cations.

A clear contribution of chemical expansion was observed for the LSCFZ series from ~450 °C, see Figure 6 and 7, due to the oxygen vacancy concentration. The increase of the TEC is substantial, going from a value of ~15 to ~23 × 10⁻⁶ K⁻¹ for $x = 0.5$ in the temperature interval between 450 and 900 °C. This behaviour is in accordance to previous reports of thermal expansion for LSCF4628 [23]. Although it is well known that chemical expansion is related to the reduction of the B-cation to lower-valence state with higher ionic radii in a response to the increasing oxygen vacancy concentration upon heating, this alone is not sufficient to model experimental data. The thermal expansion of La_{1-x}Sr_xCoO_{3-δ} (LSC) and La_{1-x}Sr_xFeO_{3-δ} (LSF) has previously been investigated in an attempt to separate and quantify the thermal and chemical contributions to the expansion [24-26]. Chen and Grande showed that the chemical expansion of both LSC and LSF was highly anisotropic in the temperature window between the onset of chemical expansion and the rhombohedral to cubic phase transition. The chemical expansion along the *c_h*-axis was more pronounced compared to the *a_h*-axis. This was rationalized by the rectification of the antiferrodistortive rotation, leading to a decompression of the MO_{6/2} (M = Co, Fe) octahedra along the *c_h*-axis. The antiferrodistortive rotation was also found to be strongly linked to the oxygen nonstoichiometry, demonstrating the link between oxygen vacancies and chemical expansion. These results indicate that chemical expansion depend as much, if not more, on the relaxation of lattice strains due to vacancy ordering effects, as on the change in ionic radii upon reduction of Co or Fe, and it is clear that any significant ionic conductivity is followed by chemical expansion. This may well be a problem which is hard to circumvent, although careful manipulation of the microstructure and low operational temperatures may diminish the critical degradation induced by chemical expansion.

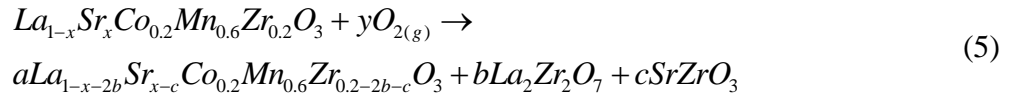
As shown in Figure 8 and 9, the LSCMZ series was found as multiphase materials. Based on the results from the Rietveld refinement analysis of the XRD-patterns in Figure 8, a heterogeneous phase equilibrium was proposed for $x = 0.1$ and 0.3. Assuming that ZrO₂ is found in either La₂Zr₂O₇ or SrZrO₃, the content of the secondary phase can be estimated, see Eq. (3) and (4).





The molar phase fractions were estimated from the Rietveld refinement and found to be in good agreement with Eqs. (3) and (4), suggesting that ZrO₂ indeed are found mainly in the secondary phases.

For x = 0.2 and 0.25, a theoretical estimation of the molar fractions became more challenging by the simultaneous presence of La₂Zr₂O₇ and SrZrO₃. The mass balance for x = 0.2 and 0.25 can be expressed as:



By assuming all ZrO₂ is found in the secondary phases, an estimation of the values for b and c could be made based on the Rietveld refinements. However, the values obtained did not fulfil Eq. (5) suggesting some ZrO₂ may be present in the perovskite phase.

The lack of solubility in the (1-x) LaCo_{0.2}Mn_{0.6}Zr_{0.2}O₃ - x SrCo_{0.2}Mn_{0.6}Zr_{0.2}O₃ system is at first glance surprising considering the full solubility of the similar system with Fe instead of Mn. The lack of solubility could be related to the unit cell size difference, with LaMnO₃ being smaller than LaFeO₃. This is, however, unlikely since Zr-solubility is reported for LaCoO₃ which has a smaller unit cell than LaMnO₃. The lack of solubility is most likely related to the higher oxidation potential of Mn³⁺ when compared to Fe³⁺. Eqs. (3) and (4) describes the mass balance of the precipitation of La₂Zr₂O₇ and SrZrO₃, and both reactions are likely to increase the oxidation state of Mn. For low Sr-content, the secondary phase precipitated is La₂Zr₂O₇. As the activity of Sr increases with the Sr-content, the secondary phase present at higher Sr-content is SrZrO₃. For the materials with Sr-content = 0.2 and 0.25, both secondary phases coexist. This correlates well with previous reports where the reactivity of La_{1-x}Sr_xMnO_{3+δ} (LSM) vs. Zr_{1-x}Y_xO_{2-δ} (YSZ) was shown to be at a minimum for similar Sr-content [27]. The activity of La and Sr will again correlate with the A/B ratio as well as the oxygen hyperstoichiometry, as reported by Yokokawa *et al.* [28].

High-valence refractory cations such as Nb⁵⁺, Ta⁵⁺, Mo⁶⁺, W⁶⁺ and Zr⁴⁺ are often not considered for substitution in IT-SOFC cathode materials due to their insulating properties. This study has demonstrated that Zr⁴⁺-substitution can be utilized to stabilize the crystal structure, prevent oxygen defect-clustering, while still retaining sufficiently low ASR by tailoring the stoichiometry and optimizing the concentration of oxygen defects and electronic charge carriers. Further research is necessary, but Zr⁴⁺ substitutions shows great promise and could be very beneficial for the development of new cathode materials for IT-SOFCs.

Conclusions

La_{1-x}Sr_xCo_{0.2}Fe_{0.6}Zr_{0.2}O_{3-δ} (0.1 ≤ x ≤ 1.0) and La_{1-x}Sr_xCo_{0.2}Mn_{0.6}Zr_{0.2}O_{3-δ} (x = 0.1, 0.2, 0.25, 0.3) were prepared via a solid state method. The crystal structure of LSCFZ was indexed to orthorhombic *Pbnm*, *Ibmm* or cubic *Pm $\bar{3}m$* depending on the level of Sr-substitution. Electrical

conductivity was found to increase with increasing Sr-substitution, reaching a maximum for $x = 0.5$. Further Sr-substitution decreased the electrical conductivity, but the area specific resistance (ASR) was shown to decrease for higher Sr-content due to the increasing concentration of oxygen vacancies. The Zr-substitution is suggested to increase the structural stability and inhibit oxygen vacancy ordering. This is rationalized by the local perturbations induced in the crystal structure due to strong Zr-O bonds. The electrical performance of $\text{La}_{0.3}\text{Sr}_{0.7}\text{Co}_{0.2}\text{Fe}_{0.6}\text{Zr}_{0.2}\text{O}_{3-\delta}$, with an ASR of $0.53 \Omega\text{cm}^2$ at 600°C , is promising in comparison to the much studied cathode material $\text{La}_{0.4}\text{Sr}_{0.6}\text{Co}_{0.2}\text{Fe}_{0.8}\text{O}_{3-\delta}$. Finally, the lack of stability of the Mn-containing samples LSCMZ in air was rationalized by the higher oxidation potential of Mn^{3+} compared to Fe^{3+} .

Acknowledgements

Financial support of the Research Council of Norway (RENERGY, grant no. 185322, Stack technology for ceramic proton conductors) is acknowledged.

References

- [1] J.W. Fergus, *Mater. Sci. Eng., A* **397** (2005) (1-2) 271.
- [2] J.M. Ralph, C. Rossignol, R. Kumar, *J. Electrochem. Soc.* **150** (2003) (11) A1518.
- [3] J.W. Stevenson, T.R. Armstrong, R.D. Carneim, L.R. Pederson, W.J. Weber, *J. Electrochem. Soc.* **143** (1996) (9) 2722.
- [4] L.W. Tai, M.M. Nasrallah, H.U. Anderson, D.M. Sparlin, S.R. Sehlin, *Solid State Ionics* **76** (1995) (3-4) 259.
- [5] L.W. Tai, M.M. Nasrallah, H.U. Anderson, D.M. Sparlin, S.R. Sehlin, *Solid State Ionics* **76** (1995) (3-4) 273.
- [6] Y. Teraoka, H.M. Zhang, K. Okamoto, N. Yamazoe, *Mater. Res. Bull.* **23** (1988) (1) 51.
- [7] H.M. Zhang, Y. Shimizu, Y. Teraoka, N. Miura, N. Yamazoe, *J. Catal.* **121** (1990) (2) 432.
- [8] J.A. Bahteeva, I.A. Leonidov, M.V. Patrakeeve, E.B. Mitberg, V.L. Kozhevnikov, K.R. Poepelmeier, *J. Solid State Electrochem.* **8** (2004) (9) 578.
- [9] V.V. Kharton, A.V. Kovalevsk, M.V. Patrakeeve, E.V. Tsipis, A.P. Viskup, V.A. Kolotygin, A.A. Yaremchenko, A.L. Shaula, E.A. Kiselev, J.C. Waerenborgh, *Chem. Mater.* **20** (2008) (20) 6457.
- [10] E.V. Tsipis, M.V. Patrakeeve, V. Kharton, A.A. Yaremchenko, G.C. Mather, A.L. Shaula, I.A. Leonidov, V.L. Kozhevnikov, J.R. Frade, *Solid State Sci* **7** (2005) (4) 355.
- [11] V. Øygarden, T. Grande, *Dalton Transactions* **42** (2013) (8) 2704.
- [12] V. Øygarden, H.L. Lein, T. Grande, *J. Solid State Chem.* **192** (2012) 246.
- [13] F.A. Kroger, H.J. Vink, *Solid State Physics-Adv. Res. Appl.* **3** (1956) 307.
- [14] E.P. Murray, M.J. Sever, S.A. Barnett, *Solid State Ionics* **148** (2002) (1-2) 27.
- [15] A. Fossdal, M. Menon, I. Waernhus, K. Wiik, M.A. Einarsrud, T. Grande, *J. Am. Ceram. Soc.* **87** (2004) (10) 1952.
- [16] P.J. Saines, B.J. Kennedy, R.I. Smith, *Mater. Res. Bull.* **44** (2009) (4) 874.
- [17] C.J. Howard, H.T. Stokes, *Acta Crystallogr B* **54** (1998) 782.
- [18] M. Avdeev, E.N. Caspi, S. Yakovlev, *Acta Crystallogr B* **63** (2007) 363.
- [19] T. Holstein, *Annals of Physics* **8** (1959) (3) 325.
- [20] T. Holstein, *Annals of Physics* **8** (1959) (3) 343.
- [21] J.B. Goodenough, *Localized to Itinerant Electronic Transition in Perovskite Oxides*, Springer (2001).

- [22] M.V. Patrakeev, A.A. Markov, I.A. Leonidov, V.L. Kozhevnikov, V.V. Kharton, *Solid State Ionics* **177** (2006) (19-25) 1757.
- [23] K. Swierczek, *Solid State Ionics* **179** (2008) (1-6) 126.
- [24] X.Y. Chen, J.S. Yu, S.B. Adler, *Chem. Mater.* **17** (2005) (17) 4537.
- [25] X.Z. Chen, T. Grande, *Chem. Mater.* **25** (2013) (16) 3296.
- [26] X.Z. Chen, T. Grande, *Chem. Mater.* **25** (2013) (6) 927.
- [27] K. Wiik, C.R. Schmidt, S. Faaland, S. Shamsili, M.A. Einarsrud, T. Grande, *J. Am. Ceram. Soc.* **82** (1999) (3) 721.
- [28] H. Yokokawa, N. Sakai, T. Kawada, M. Dokiya, *Solid State Ionics* **52** (1992) (1-3) 43.